Macromolecules
ARTICLE

Macromolecules **2009**, *42*, 7137–7145 **7137**
DOI: 10.1021/ma9003242

Dependence of Self-Assembled Peptide Hydrogel Network Structure on Local Fibril Nanostructure

Rohan A. Hule,[†,⊥] Radhika P. Nagarkar,[‡] Boualem Hammouda,[§] Joel P. Schneider,[‡] and Darrin J. Pochan*[,†]

[†]*Department of Materials Science and Engineering and Delaware Biotechnology Institute, University of Delaware, Newark, Delaware 19716,* [‡]*Department of Chemistry and Biochemistry, University of Delaware, Newark, Delaware 19716, and* [§]*National Institute of Standards and Technology, 100 Bureau Drive, Gaithersburg, Maryland 20899-6102.* [⊥]*Current address: Division of Chemistry and Chemical Engineering, California Institute of Technology, 210-41, Pasadena, CA 91125.*

Received February 12, 2009; Revised Manuscript Received July 16, 2009

ABSTRACT: Physically cross-linked, fibrillar hydrogel networks are formed by the self-assembly of β-hairpin peptide molecules with varying degrees of strand asymmetry. The peptide registry in the self-assembled state can be used as a design element to generate fibrils with twisting, nontwisting, or laminated morphology. The mass density of the networks varies significantly, and can be directly related to the local fibrillar morphology as evidenced by small angle neutron scattering (SANS) and *in situ* substantiation using cryogenic transmission electron microscopy (cryo-TEM) under identical concentrations and conditions. Similarly, the density of the network is dependent on changes in the peptide concentration. Bulk rheological properties of the hydrogels can be correlated to the fibrillar nanostructure, with the stiffer, laminated fibrils forming networks with a higher G' as compared to the flexible, singular fibrillar networks.

Introduction

The nanostructure−network relationships of polymer gels[1−4] and semiflexible networks,[3,5−11] biological systems,[12−15] polyelectrolyte gels,[16−18] and wormlike micellar networks[19−21] have been studied rigorously, both theoretically and experimentally. A common thread binding these molecularly disparate systems is the scattering behavior of the semiflexible chains and the networks they form. It is widely accepted that network rheological properties, solute diffusion within a network, local chain dynamics, and nature of entanglements are affected by changes in the overall network morphology. In addition, biological properties dependent on network mechanical properties such as cell viability,[22] adhesion,[23] and motility[24] are affected as a result of the nanostructure. A thorough study of the properties of the network constituent chains themselves, and the multichain structure they form, can lead to an understanding of the gel structure−property relationships and potential in vitro and in vivo biological usage. In this paper, the self-assembly of oligopeptide sequences that fold intramolecularly into amphiphilic, asymmetric β-hairpins and intermolecularly into fibrillar nanostructures previously reported by Nagarkar et al. has been used as a fundamental mechanism for creating hydrogel networks.[25] Fibrils were designed to have distinct nanostructures by rationally tailoring the synthetic peptide chemistry. Scattering exponents from the local fibrillar structure as well as the overall network extracted via SANS are related directly to the discrete nanomorphology as seen in situ in cryogenic TEM as well as bulk hydrogel properties studied by rheology. Rational peptide design provides the ability to tune morphology on the nanoscale in order to control macroscopic material properties.

Hydrogels are proving to be an excellent class of materials in the biomedical arena. They have found extensive usage in tissue engineering efforts as extracellular matrix substitutes,[26−28] wound sealants,[29,30] and templates for inorganic−organic nanocomposites.[31,32] For example, preformed hydrogels used to treat defects in animal models can be potentially used in humans.[33−35] Hydrogels that form via sol−gel transitions due to in vivo triggers[36,37] or photo-cross-linking[38,39] offer the possibility of minimally invasive surgery. The origin of such versatile usage lies in control over the final properties, achieved in turn through the gel nanostructure and chemistry. Among the methods used for hydrogel structure−property comprehension, neutron scattering and electron microscopy have emerged as indispensable tools. Used in combination, they help study structures that span 4 decades in length scale from angstroms to micrometers in reciprocal and real space, respectively. Global and quantitative morphological analysis offered by scattering can be combined effectively with microscopic data over equivalent length scales in real space. Herein, we rely on empirical fitting methods to connect hydrogel network densities and their nanostructures to in situ morphology seen via cryo-TEM at identical concentrations and conditions, a novel method to relate the trends studied using these two experimental routes.

We have reported earlier on the self-assembly of a synthetic, 20 amino acid peptide (MAX1) that was designed to undergo triggered, intramolecular folding, under specific aqueous conditions, and concomitant intermolecular self-assembly into a rigid hydrogel network.[40,41] The self-assembled network consists of well-defined fibrils, monodisperse in cross section, and displays rheological properties similar to physically cross-linked, semiflexible biopolymer networks.[42] MAX1 [$(VK)_4$-V^DPPT-$(KV)_4$-NH_2] consists of two strands of alternating valine (V) and lysine (K) residues flanking a central type II′ β-turn region[43] (V^DPPT) that folds into a facially amphiphilic β-hairpin structure once initiated by an appropriate trigger such as pH,[41] temperature,[40] or ionic strength.[44] Once folded, the hairpin structure consists of two symmetric β-sheet strands flanking the central turn sequence.[45] Numerous hairpins assemble, both laterally, primarily due to hydrogen bonding and, facially, due to collapse of valine-rich faces in the folded state to form fibrils that have a homogeneous cross section with ∼3 nm diameter. On the basis of this parent MAX1 sequence, we have recently introduced a new peptide design by rationally altering the placement

*Corresponding author. E-mail: pochan@udel.edu.

© 2009 American Chemical Society
Published on Web 08/27/2009

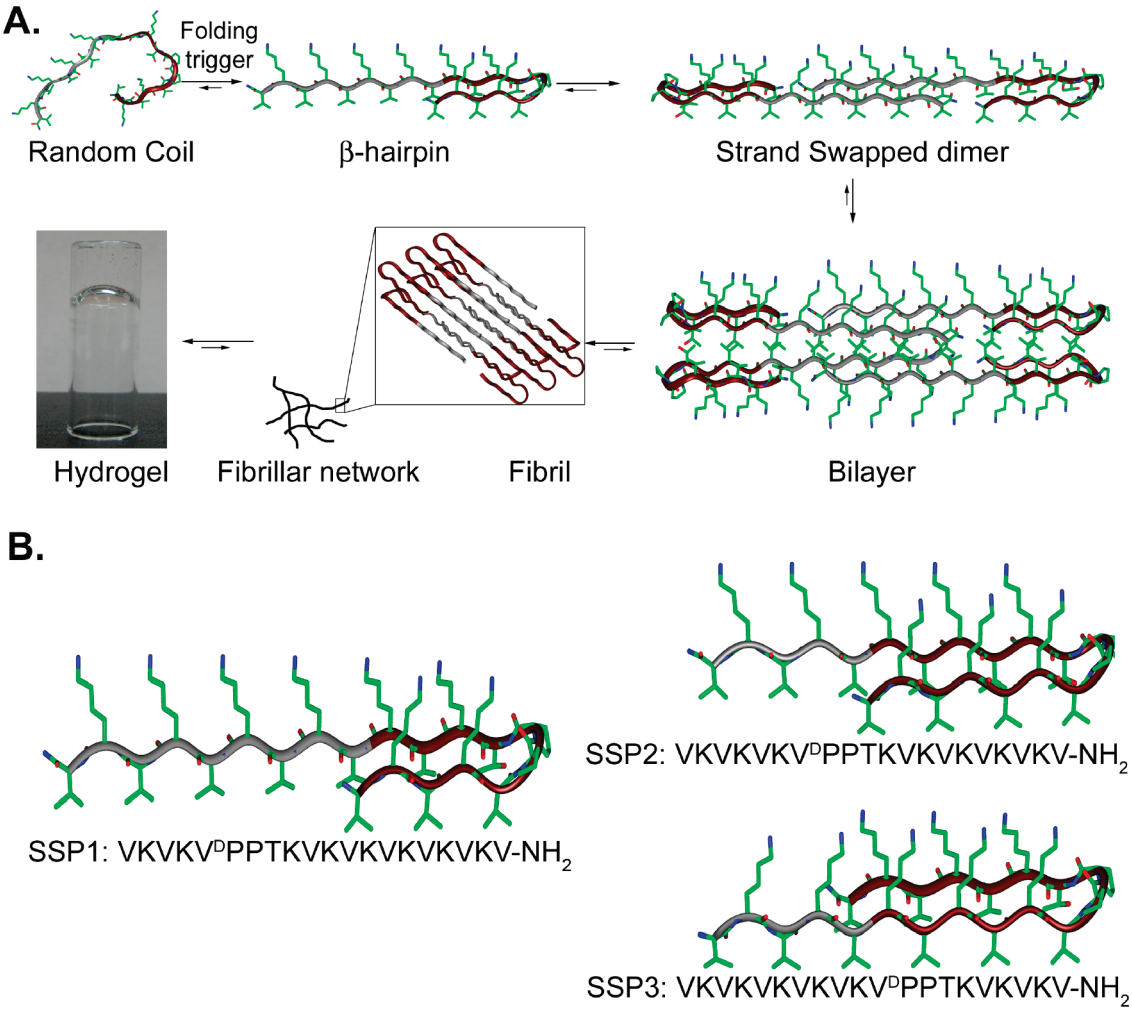

Figure 1. (A) Schematic for the strand-swapping self-assembly mechanism for the peptides SSP1, SSP2, and SSP3. (B) Peptide sequences of SSP1, SSP2, and SSP3 along with their corresponding β-hairpin illustrations.

of this turn region in the sequence of MAX1 in such a way so as to introduce strand asymmetry within the folded β-hairpin.[25] Integration of strand asymmetry enables the peptide to exchange strands with another β-hairpin, as seen in Figure 1A. Such exchanges may potentially be stabilized by hydrogen bonds formed between the backbones of the swapped strand regions of the two β-hairpins. The peptides remain unfolded when dissolved in an aqueous solution. However, the introduction of a pH trigger (125 mM borate buffer at pH 9, 10 mM NaCl) leads to the partial deprotonation of the lysine side chains, allowing the sequence to fold into a facially amphiphilic β-hairpin conformation. Two peptide sequences with varying degree of β-strand asymmetry were previously designed: SSP1 [$(VK)_2$-$V^{D}PPT$-$(KV)_6$-NH_2] and SSP2 [$(VK)_3$-$V^{D}PPT$-$(KV)_5$-NH_2] such that the folded hairpin displays an exchangeable strand region that can be swapped with another β-hairpin to form a facially amphiphilic dimer. This leads to concomitant facial self-assembly wherein the valine-rich hydrophobic faces of two such dimers collapse to form a bilayer. Extensive intermolecular hydrogen bonding as well as van der Waals contacts between numerous such collapsed, strand-swapped dimers facilitates lateral self-assembly to form a fibrillar nanostructure that forms a self-supporting 3D hydrogel, as seen in Figure 1. Herein, we introduce a third peptide sequence SSP3 [$(VK)_5$-$V^{D}PPT$-$(KV)_3$-NH_2], isostructural to SSP2 in terms of the strand asymmetry, but whose strand registry is switched relative to SSP2 such that now the N-terminal strand is exchanged instead of the C-terminal strand. It should be noted that the total number of amino acids in all these peptide sequences remains the same at 20.

We aim to exploit the nanoscale morphological control exhibited by these three peptides to understand the physics of the self-assembly, in terms of scattering parameters such as correlation lengths and scattering exponents at widely differing length scales, and associate these factors with bulk rheological properties of the hydrogel. All SANS measurements have been suitably supported by cryo-TEM data that enable direct, *in situ* visualization of the system at identical concentrations and conditions, a unique feature for self-assembled peptidic hydrogels. Thus, the precisely tunable peptide nanostructures, combined with quantitative scattering characterization, may comprise a model semiflexible network system to directly probe the relationship between peptide design and network properties that may ultimately lead to a more thorough understanding of biomolecular network behavior in general.

Results and Discussion

The self-assembled fibrillar nanostructures for this set of asymmetric peptides, along with a schematic illustrating the three distinct nanostructures resulting from the three respective peptides, are shown in Figure 2. As seen from the negatively stained TEM micrographs (Figure 2A−C), a change in the peptide registry affects the local fibrillar morphology substantially; the SSP1 scaffold is constituted of fibrils with a regular, repeated twist, and SSP2 forms singular, untwisted fibrils, while SSP3 is comprised of laminated fibrils. The nontwisted and twisted fibrillar morphologies were conserved throughout the grid across

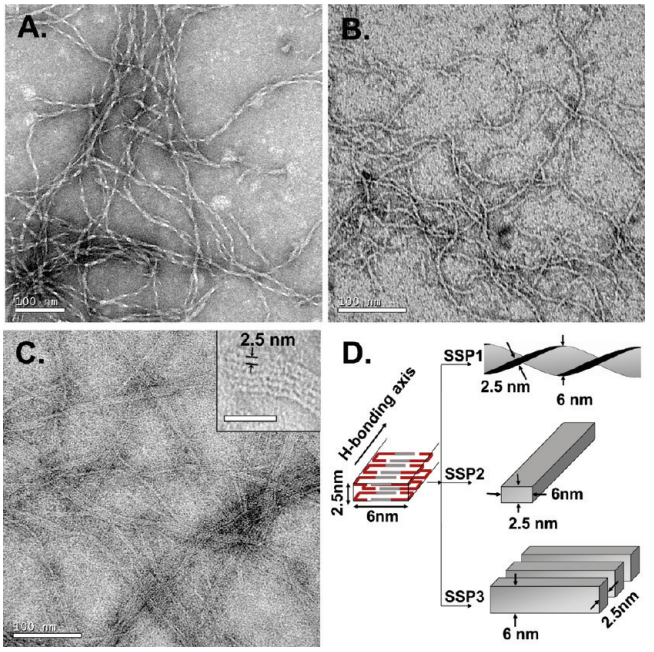

Figure 2. TEM micrographs of SSP1 (A), SSP2 (B), and SSP3 (C) and a schematic (D) comparing the three fibrillar nanostructures from an identical self-assembled bilayer. The scale bar for panels A−C is 100 nm. The scale bar for the inset in panel C is 20 nm.

several samples and remained unchanged with time for periods of at least several weeks. In case of the laminated fibrils, the number of individual filaments that stack together in a laminate is variable and is dependent on the self-assembly conditions.

Small-angle neutron scattering (SANS) was used to globally quantify the hydrogel morphology, both at the network (100s of nanometers) as well as the fibrillar (1−10 nm) length scales. A review of the analysis used herein along with a detailed discussion of the rationale used is necessary before delving into the results and their interpretation. As pointed out earlier, SANS in combination with cryo-TEM has been utilized to understand changes in the network densities of these materials. The peptidic self-assembled hydrogels presented in this paper are more akin to percolated networks of well-defined nanostructures such as those composed of carbon nanotubes and clays as opposed to traditional, molecular hydrogel networks. Schaefer et al.[46,47] and Schmidt et al.,[48,49] among others, have utilized power-law and scaling exponent fits at low as well as high Q scattering regimes to extract morphological information on carbon nanotube and clay dispersions and polymer networks.[50−52] It is important to distinguish such permanent networks that often display similar scaling of mass density of nanostructure within specific, finite Q regimes from fractals, objects that display such self-similarity in both geometry and mass over many decades in Q. Strictly speaking, systems exhibiting specific mass density over a given Q regime need not be fractal. The lack of multiple length scale scaling or self-similarity in systems such as carbon nanotubes and clays has been primarily ascribed to the experimental uncertainties in achieving a well-dispersed state. For instance, poor solubility in nanotube and clay dispersions[50] and aggregation tendencies in hydrogels may negate well-defined, identical scaling of mass over multiple length scales. Scattering data similar to that seen in this current study cannot be adequately described by a single expression over the entire Q regime; instead, it is often a superposition of distinct scaling trends.[53,54] However, while not fractal in the strictest sense of being self-similar over multiple length scales, peptide hydrogel networks displaying fractional scaling of mass over a limited Q range contain crucial information in terms of network density that is dependent on the peptide, self-assembly behavior, and local nanostructure that dictates the final properties of these materials. In this paper, we have attempted to extract differences in network densities, mass scaling, and local self-assembled states at distinct length scales and relate these to in situ morphological evidence collected using cryogenic TEM under identical length scales, concentrations, and conditions. The presence of equivalent, in situ evidence renders a greater degree of confidence to trends and interpretations obtained via scattering. Such a direct comparison of reciprocal and real space may prove key in facilitating future network-nanostructure correlations in other semiflexible networks.

The scattering profiles of the hydrogels were fit to the following functional form:

$$I(Q) = A/Q^n + C/[1+(QL)^m] + B$$

For the purpose of this study, the first term, A/Q^n, describes scattering from the gel network in the low Q regime, whereas the second term, $C/[1 + (QL)^m]$, describes high Q scattering, where $Q=(4\pi/\lambda)\sin(\theta/2)$.[55] A nonlinear, least-squares fit was performed on the functional form to obtain the multiplicative factors of the first and second terms (A and C, respectively), the Q-independent background scattering (B), the correlation length (L), and the low Q (n) and high Q (m) scaling exponents. Similar functional forms have been successfully employed to describe diverse systems including similar peptide-based hydrogels,[56] clustering and solvation characteristics of polymer[57] and polyelectrolyte[58] solutions, and other biophysical systems.[12] The scattering profiles for SSP1, SSP2, and SSP3 at 1 wt % can be seen in Figure 3. The hydrogel structure on the network length scales (100s of nanometers) can be understood from the low Q scattering exponent (n). It is seen that all peptide gels have a value of $n = 1.7$ indicative of scattering from fully swollen Gaussian chains in a good solvent.[59] Hence, varying the degree of strand asymmetry from a strand swap region composed of 8 residues in SSP1 to 4 residues in SSP2 does not affect network scattering. Similarly, altering the placement of the longer strand from the C terminus in SSP2 to the N terminus in SSP3 also does not affect scattering in the low Q regime. Similar swollen chain behavior has also been predicted by a power-law decay analysis of fibrillar assemblies of oligopeptide-based hydrogels that revealed identical exponents in the low Q region.[60] However, a closer look at the network nanostructures of these peptides as seen in Figure 2 (negatively stained TEM) and Figure 5 (cryo-TEM, *vide infra*) suggests that while well-swollen, flexible fibrillar nanostructure may be a good description for SSP1 and SSP2 network structure, it does not faithfully represent the network structure of SSP3, the fibrils of which are clearly laminated and thus stiff over distances up to 1 μm. This example serves to highlight the need to understand such complex, self-assembled networks using a combination of tools that probe both reciprocal and real space.

Calculation of the individual fibril dimensions and corroborating it with a detailed self-assembly mechanism can be done for SSP1 and SSP2.[25,61,62] Variation in the overall fibrillar width due to differing degree of lamination prevents a similar analysis being employed for SSP3. Moreover, a weak peak can be seen at $Q = 0.22$ Å^{-1} ($d = 28$ Å) in the scattering curve for SSP3. In the absence of microscopic data, such subtle scattering features can easily be misinterpreted to arise from correlations between the self-assembling peptide molecules. However, it is apparent from negatively stained TEM data (Figure 2C) that this d-spacing can be attributed to the width of a single filament within a stack of multiple filaments constituting a laminate. Moreover, this d-spacing agrees well with the theoretical calculation for a bilayer thickness from peptide models, shown in Figure 1A. This evidence, in addition to fibrillar heights measured via AFM (refer to Supporting Information, Figure S-2), corroborates an

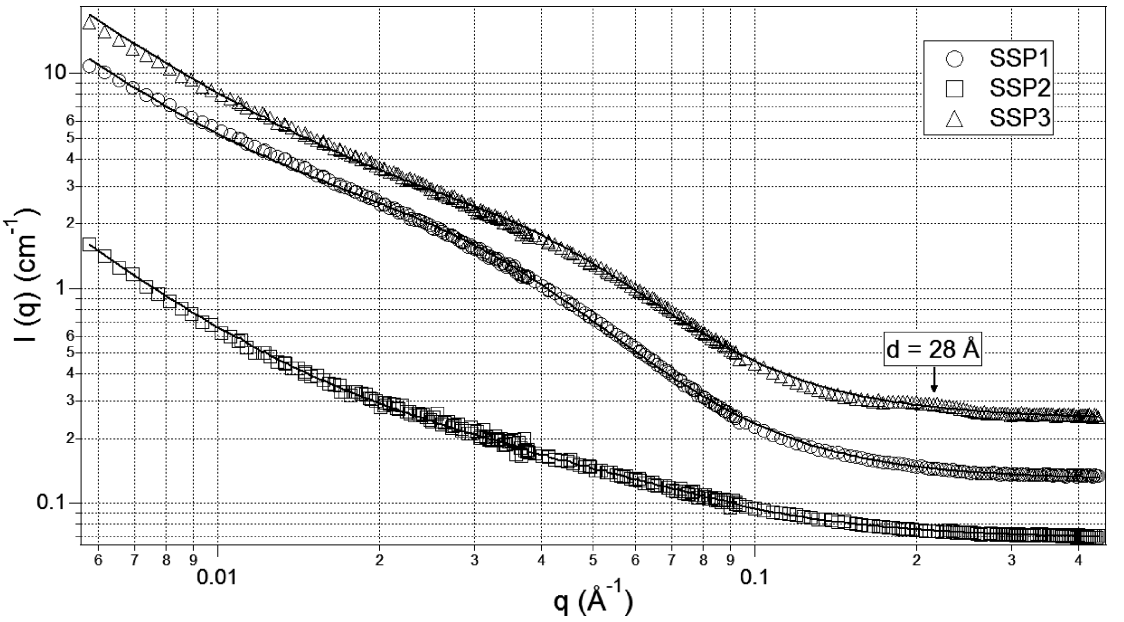

Figure 3. SANS data for 1 wt % SSP1 (○), SSP2 (□), and SSP3 (△) hydrogels triggered by pH 9, 125 mM Borate, 10 mM NaCl buffer in D_2O. The solid lines are the fits to the functional form. The weak peak seen in the high Q regime for SSP3 corresponding to a spacing of 28 Å agrees well with the thickness of a β-sheet peptide bilayer and is additional evidence in support of the strand swapping mechanism. Intensities have been offset for clarity.

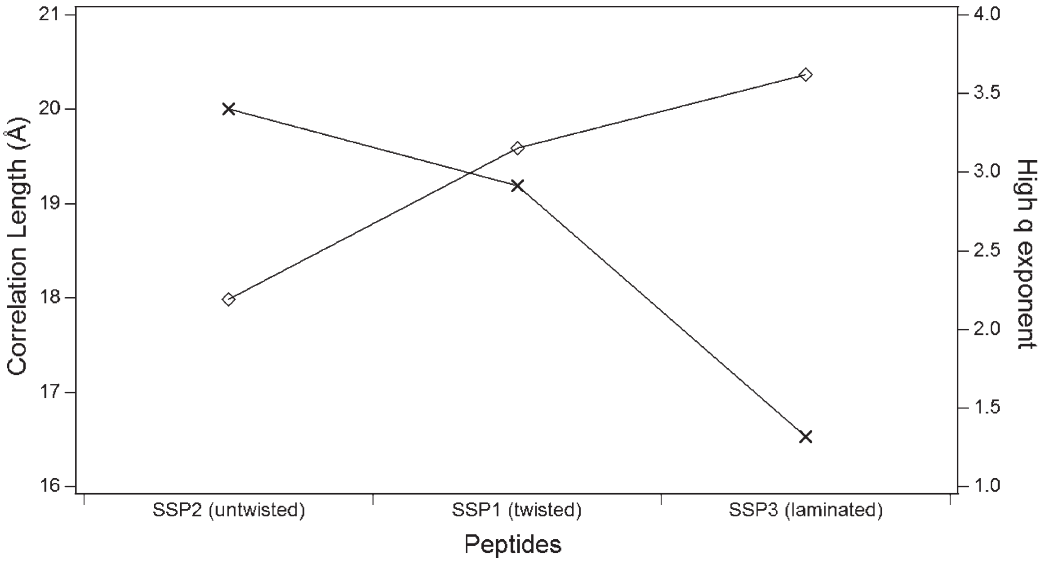

Figure 4. Trends for correlation length, L (×), and the high Q exponent, m (◇), for all three peptides at 1 wt %.

identical strand-swapping self-assembly mechanism for SSP3 as observed in SSP1 and SSP2. As discussed earlier, such information extracted from inverse space can be appropriately supported by direct observation using microscopic techniques.

Beyond the similarities between the three peptidic nanostructures just discussed, the nanoscale morphological differences among the three peptides are also reflected in their scattering profiles. As mentioned earlier, SSP2 forms untwisted fibrils whereas SSP1 and SSP3 gels are comprised of twisted and laminated fibrils, respectively. A laminated fibrillar morphology is locally more compact/denser than a twisted one, which, in turn, is more compact as compared to an untwisted fibril. Increasing compactness reflects the higher number of peptide molecules per unit length of these three fibrillar nanostructures. The fact that SSP1 and SSP3 have higher scattering intensities than SSP2 in the mid-to-high Q regimes is further evidence of the increasing number of scattering centers that arise as a result of the compactness. The values from the fits for the high Q exponent, m, for these three peptides support the trend observed for the compactness of the self-assembled fibrils (Figure 4). SSP2 has a high Q exponent of 2.19. This value increases to 3.15 for SSP1, signifying a denser association of the peptide molecules and of the local fibrillar network. On the other hand, the high Q exponent for SSP3 is 3.62, representing power law scattering from an interface.[53,54] It is likely that the laminating, stiff fibrils of SSP3 offer this defined interface between the laminate and surrounding solvent. Hammouda et al. have similarly inferred stiffening of the polymer chain and, therefore, a greater degree of compactness due to an increasing scattering exponent value from 1.67 to 3.7 in other systems.[12] We have also observed comparable changes in the high Q exponent in other peptide-based[56] and hyaluronic acid-based[63] hydrogels. The higher compactness of the fibrillar nanostructure can also be monitored as a function of the correlation length, L. The correlation length decreases from 20 Å for SSP2 to 16 Å for SSP3.

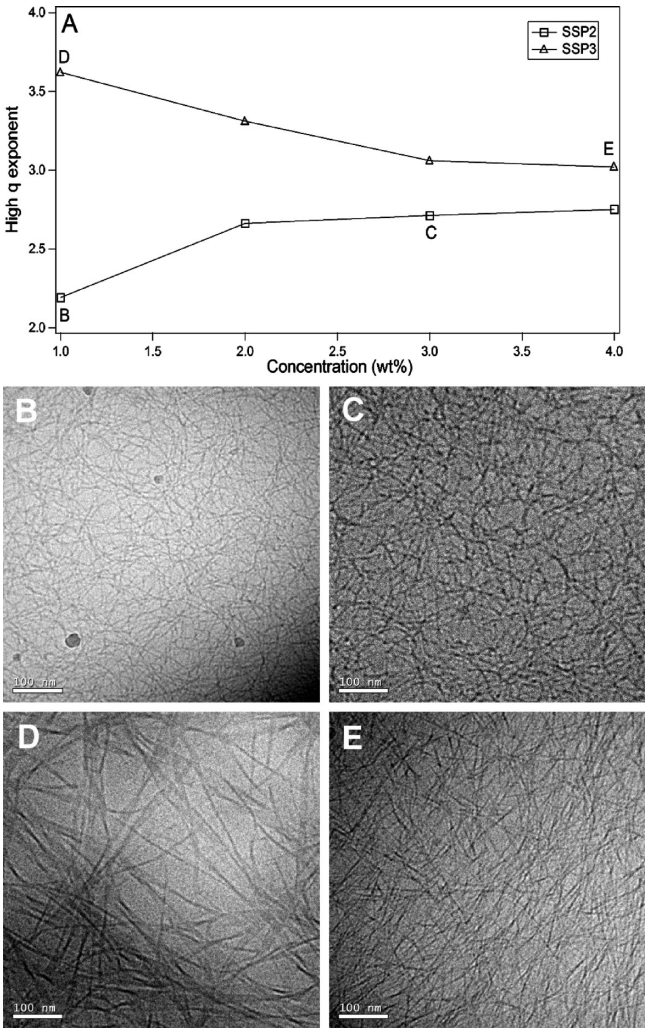

Figure 5. (A) Variation of the high Q exponent, m, with concentration for SSP2 (□) and SSP3 (△). Cryo-TEM micrographs representing the *in situ* hydrogel nanostructure of SSP2 (B, C) and SSP3 (D, E) at 1 wt % (B, D) and 4 wt % (C, E), respectively. The scale bar for panels B−E is 100 nm.

A decrease in the correlation length is indicative of closer packing of the peptide molecules and, therefore, a higher degree of compactness within the fibrillar nanostructure. A comparable increase in the correlation lengths of double-stranded DNA from 8.5 to12.3 Å during its denaturation from the helix to the coil phase was attributed to easier transmission of correlations through flexible coils, as compared to the rigid helix.[12] Similar interpretations have also been made in clustering solutions of poly(ethylene oxide).[57]

These strand-swapping hydrogels show significant differences in their scattering profiles with concentration. An increase in the peptide concentration from 1 to 4 wt % results in denser hydrogel networks. Although an increase in the concentration leads to higher storage moduli (data not shown) for hydrogels of all peptides due to greater number of fibrillar cross-links, there is also a distinct change in the scaling behavior of the self-assembled fibrils and local fibrillar networks obtained from SSP2 (nontwisted, singular) and SSP3 (nontwisted, laminated). This transition can be accurately mapped by monitoring the high Q exponent (m) as a function of concentration as shown in Figure 5A for SSP2 and SSP3. SSP2 shows an increase in the scattering exponent from 2.19 at 1 wt % to 2.71 at 3 wt % to 2.75 at 4 wt %. The increasing value of the exponent in this Q regime is indicative of the SSP2 hydrogels becoming more compact/dense with concentration. At higher concentrations, a higher density of self-assembled fibrils leads to greater number of cross-links and therefore smaller interfibrillar distances within the network. The increase in the number and cross-linking density of the fibrils appears as an increase in the high Q scattering exponent. Moving from reciprocal to real space, the nanostructure of the hydrogels and change in the density of the network under identical parameter variations as SANS can be visualized directly by cryo-TEM. Cryo-TEM[64−66] enables *in situ* imaging of the hydrogel matrix as shown in Figure 5B−E. The gray areas are vitrified water while the dark regions are the nanoscale morphology of the self-assembled peptide. Thus, cryo-TEM enables direct comparison of the network behavior to the SANS data at the same concentrations, a useful feature for the comprehensive elucidation of the physics of these semiflexible networks. Cryo-TEM supports the untwisted nature of SSP2 fibrils and the increase in the number of fibrils from 1 to 3 wt % as revealed by SANS, seen in Figure 5B,C (see Supporting Information for image analysis proving a decrease in the mean distance between interfibrillar crosslinks, Figure S-1). The increasing density of the fibrillar network leads to a more compact network and appears as an increase in the high Q scattering exponent, as observed in the SANS data.

Interesting changes in the high Q exponent can be seen for SSP3, the peptide with laminating fibrils, as it goes through an identical concentration gradient. As seen in Figure 5A, the high Q exponent, m, decreases from 3.62 at 1 wt % to 3 at 4 wt % in case of SSP3. As mentioned earlier, the defined surfaces of stiff, laminated fibrillar bundles offer a defined interface between the fibrils and the surrounding solvent. This interface is the origin of the high Q power-law scaling observed for SSP3 at low concentrations. The transition in the mass scaling behavior that affects the local network density of the SSP3 laminated fibrillar network can be explained based on the kinetics of the self-assembly process. The self-assembly process in SSP3 involves the formation of a facially amphiphilic dimer due to intermolecular hydrogen bonding between the swapped region of two folded, asymmetric β-hairpins. Two such dimers associate to form a four-hairpin bilayer, primarily driven by the collapse of their hydrophobic faces composed of valines. Numerous such bilayers associate laterally through intermolecular hydrogen bonding to form a single filament. Several filaments undergo higher order assembly to give rise to a laminated fibril. An increase in the concentration of the peptide results in faster kinetics of this self-assembly mechanism, a process that leads to imperfections in the peptide bilayer. Evidence suggests that these imperfections are formed by mispacking of the hydrophobic portions of the peptide molecules in the bilayer. It has been seen in similar peptidic systems that such imperfections in the bilayer serve as nucleation points for branching fibrils, clearly seen via cryo-TEM.[67] Such defects in the bilayer disrupt the regular lamination in SSP3, thus leading to a lower degree of lamination in the overall network. A reduction in the degree of lamination, coupled with the enhancement in local fibrillar network density, results in poor definition of the interface between individual fibrils and the solvent. Thus, an increasingly rough interface between the fibrillar laminates and solvent with concentration may be ascribed to be the origin of the decrease in the high Q scaling exponent of SSP3 local network. Other groups have reported comparable changes in the high Q exponent.[60] As with SSP2, the SSP3 fibrils and the scaffold they constitute are visualized *in situ* by cryo-TEM micrographs, shown in parts D and E of Figure 5 for 1 and 4 wt % peptide concentration, respectively. The laminated nature of the fibrils at 1 wt % that provide the well-defined interfaces between the fibrils and the solvent can be seen clearly in Figure 5D. Compared to SSP2 fibrils at identical concentrations (Figure 5B), these fibrils appear to have a significantly higher persistence length. As the concentration is increased to 4 wt %, a significant increase in the network density of the fibrils can be seen, leading to a denser network (Figure 5E).

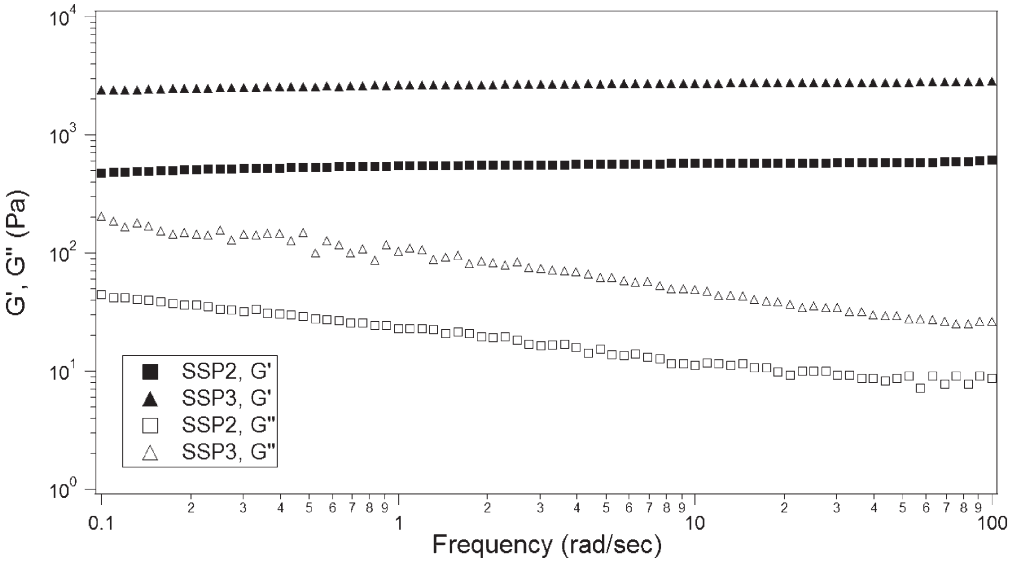

Figure 6. Frequency sweep data for SSP2 (□) and SSP3 (△) at 2 wt % peptide, pH 9, 125 mM borate, 10 mM NaCl, 50 °C. Solid and open symbols represent G' and G'', respectively.

In agreement with SANS data, the homogeneous nature of the network on the local fibrillar length scales at these concentrations can also be seen clearly. Similarly, cryo-TEM confirms a lower degree of lamination as indicated by SANS, as a result of the faster kinetics of self-assembly at higher concentrations. Homogeneity of the network due to higher fibrillar density as well as a lower degree of lamination due to faster kinetics disrupts the defined, laminated fibrillar interface and changes the scaling exponent of the network at these local network length scales.

Differences in the fibrillar morphology on the fibrillar and network length scales have a direct consequence on the bulk hydrogel material properties, as evidenced by a significant change in the rheological properties of the hydrogels consisting of nontwisted vs laminated fibrils. We chose these morphologies as they represent the two extreme cases in the variation of scattering exponents and correlation lengths, as seen in all scattering studies presented herein. Figure 6 shows the frequency sweep data for SSP2 and SSP3 at 2 wt %, 50 °C. As seen previously in similar systems,[42,56] the G' values for all gels are an order of magnitude higher than their corresponding G'' values. No crossover can be detected within the 0.1−100 rad/s frequency range. In addition, the elastic moduli are essentially frequency independent. Such rheological behavior suggests the presence of permanent junction points as opposed to transient entanglements leading to a viscoelastic plateau modulus.[3,42] As seen in Figure 6, the storage modulus of these hydrogels can be controllably altered from 2739 ± 191 Pa for the laminated SSP3 to 517 ± 40 Pa for the nontwisted SSP2. Differences in the bulk rheological properties of these hydrogels are manifested through their local morphology, which, in turn, affects the corresponding network structure. The higher stiffness of laminated SSP3 fibrils as compared to the singular, flexible SSP2 fibrils can be directly visualized in the cryo-TEM micrographs and via the high Q behavior observed in SANS, described earlier in this paper. Moreover, at identical concentrations, gels consisting of laminating fibrils have fewer interfibrillar entanglements compared to the networks formed by singular fibrils. Hence, the higher modulus of SSP3 gel can be attributed to the stiffer fibrillar morphology and its effects on the network structure as compared to the flexible fibrils of SSP2. Rheological data presented here confirm the bulk properties via a study of the network, suggesting that fibrillar nanostructure and the network morphology can be directly related and can be used to formulate materials with prerequisite mechanical characteristics. Moreover, similar gels have been proven to be excellent 3D scaffolds for cell growth and proliferation.[68] Future efforts can be directed toward extending such studies to include gel−cell scaffolds that enable determination of specific mechanical/structural−bioproperty relations such as cell adhesion and motility for potential in vivo usage.

Conclusions

Structure−property correlations in a strand-swapped, self-assembled peptidic system on the local fibrillar as well as the network length scales have been characterized by SANS, cryo-TEM, and rheology. Changes in the correlation lengths, low Q (network), and high Q (fibrillar) mass scaling exponents have been related directly to the distinct nanomorphology exhibited by this *de novo* designed peptidic system. All peptides exhibit identical scattering behavior in the low Q regime; however, electron microscopy helps distinguish the morphological differences between laminating and singular fibrillar networks. In the high Q regime, the scattering exponent reflects the fibrillar nanomorphology, varying from the singular, nontwisted SSP2 and the twisted SSP1 fibrillar networks to the relatively stiff, laminating SSP3 networks. An increase in SSP2 concentration results in a denser network and, hence, higher scaling exponent. A reduction in the power-law exponent is observed for an identical increase in SSP3 concentration and can be attributed to faster self-assembly kinetics that disrupts the well-defined, laminated fibrillar interface. Most importantly, trends seen in the reciprocal space have been substantiated in the real space by direct, *in situ* visualization of the hydrogel networks. Such a direct assessment of self-assembled peptidic hydrogel networks by SANS and cryo-TEM, studied under identical conditions and concentrations, has not been done before. This study emphasizes the relevance of utilizing a combination of scattering and microscopy for a thorough comprehension of other complex, self-assembled systems and can help reduce misinterpretations of the morphology from a scattering analysis alone. Additionally, the structure−property relationship dependence on the nanostructure has been demonstrated via rheology, with stiffer fibrillar networks resulting in hydrogels with higher moduli.

The precisely defined nanostructure of the fibrils constitutes a model semiflexible network system that may help understand and model biopolymer networks in general. For example, the overall charge of the folded hairpin can be reduced by the substitution of negatively charged residues which, in turn, leads to faster assembly kinetics and, therefore, higher number of cross-links in the

network.[68] An elevated number of cross-links leads to possible changes in the correlation length and the network scaling exponents.[56] Such controllable, densely cross-linked networks are ideal for diffusion studies or encapsulation of small molecules for drug delivery or cell encapsulation.[68] Besides self-assembled networks, the scattering model used here coupled with cryo-TEM observations may be used to study the network morphology of entangled, elongated wormlike micelles, whose behavior is reminiscent of the system discussed herein. These systems have long been known to exhibit a decrease in the viscosity and stress relaxation beyond a critical concentration, a phenomenon attributed to fluid connection points wherein micellar chains undergo reversible scission and recombination on a time scale dependent on the amphiphile, counterion concentration, and temperature.[69−71] A concentration study of such surfactants can potentially explain the fluid junction points that dictate the unique rheological behavior exhibited by these networks. Therefore, the strand-swapping peptides provide a template to study the structure−property relations of other semiflexible networks.

Experimental Section

Materials. Rink amide resin was purchased from Polymer Laboratories. 9-Fluorenylmethoxycarbonyl (Fmoc) protected amino acids with adequate side chain protection were acquired from Novabiochem. *N*-Methylpyrrolidone (NMP) was purchased from EMD Biosciences. 1*H*-Benzotriazolium-1-[bis(dimethylamino)methylene]-5-chloro,hexafluorophosphate(1-),3-oxide (HCTU) was obtained from Peptides International. Dimethylformamide, methylene chloride, acetic anhydride, acetonitrile, and methanol were purchased from Fisher. Piperidine and 1,8-diazabicyclo[5.4.0]undec-7-ene (DBU) were acquired from Aldrich. Trifluoroacetic acid, anisole, thioanisole, ethanedithiol, and D_2O were obtained from Acros Organics. Vydac analytical and semipreparative scale C18 peptide/protein column were used for purification. Deionized water having a resistivity of 18.2 MΩ·cm obtained from the Milli-Q (Millipore) purification system was used to prepare all solutions.

Peptide Synthesis and Purification. Peptides were prepared employing Fmoc-based solid phase peptide synthesis (SPPS) protocols on a ABI 433A synthesizer. SPPS was carried out on a 0.25 mmol scale using Rink amide resin (loading: 0.64 mmol/g) with HTCU coupling chemistry. 19% Piperidine, 1% DBU in NMP afforded Fmoc deprotection. Post SPPS, a cleavage reagent consisting of 95:5:3:2 TFA, thioanisole, ethanedithiol, and anisole was employed to effect resin cleavage and simultaneous side chain deprotection. The resin was separated by filtration, and the resulting reaction mixture was precipitated in cold ether to afford the crude peptide. All peptides are C-terminally amidated and possess an N-terminal free amine. Semipreparative scale reverse phase HPLC of the crude peptide employed the following gradients of solvent A (0.1% TFA in water) and solvent B (90% acetonitrile, 10% water, 0.1% TFA). For SSP1, a linear gradient was applied from 0 to 20% B in 20 min followed by an additional linear gradient of 20−100% B in 320 min. SSP1 eluted with a retention time of 45 min using this gradient. For the purifications of SSP2 and SSP3, 0% solvent B was held isocratically for 2 min, followed by linear gradients of 0−25% solvent B in 25 min and 25−100% solvent B in 150 min to elute the peptide off the column in 36 min. The purified peptide was further lyophilized and its purity assessed by analytical HPLC and electrospray ionization mass spectrometry (ESI-MS). Since the three peptides vary only in the spatial arrangement of residues in their peptide sequences, they possess identical masses, i.e., calculated $[M + 2H]^{2+} = 1115.9$. The observed m/z are as follows: SSP1, $[M + 2H]^{2+} = 1115.4$; SSP2 $[M + 2H]^{2+} = 1115.7$; SSP3 $[M + 2H]^{2+} = 1115.6$.

Hydrogel Preparation. 2 mg of a desired peptide were first dissolved in 100 μL of Milli-Q water, resulting in an aqueous peptide stock solution at room temperature. An equal volume of 250 mM borate buffer, pH 9, 20 mM NaCl was added to the stock to initiate self-assembly. This resulted in a 1 wt % hydrogel. Other concentrations (2, 3, and 4 wt %) were prepared similarly using appropriate peptide and solvent amounts.

Small-Angle Neutron Scattering (SANS). SANS experiments were performed on the 30 m instrument (NG-3)[72] at the NIST Center for Neutron Research (NCNR), National Institute of Standards and Technology (NIST), Gaithersburg, MD. Gel samples were prepared by mixing the peptide and buffer solutions, both prepared in D_2O to enable adequate contrast between the hydrogen-rich gel matrix and the deuterated solvent. Solutions were pre-equilibrated at 5 °C, mixed gently in a vial, and transferred immediately to titanium sample cells with 30 mm diameter quartz windows and a 2 mm path length. All samples were incubated overnight at room temperature prior to scattering measurements to ensure stable conditions. Monochromatic neutrons at $\lambda = 6$ Å and a wavelength spread ($\Delta\lambda/\lambda$) of 0.14 were incident on the sample. The scattered neutrons were captured on a 64 cm × 64 cm 2-D detector. Sample-to-detector distances of 1.33, 4.50, and 13.17 m were used to the study of the scattering wavevector Q in the range $0.004 < Q$ (Å^{-1}) < 0.4, defined by $Q = (4\pi/\lambda)\sin(\theta/2)$, where λ is the neutron wavelength and θ is the scattering angle. Raw data were corrected for background electronic noise and neutron radiation, detector inhomogeneity and sensitivity, and empty cell scattering. Intensities were normalized to an absolute scale using main beam transmission measurements and were reduced according to published protocol.[73] The error bars of the data points for all SANS plots are within the limits of the symbols.

Transmission Electron Microscopy. Bright field images of diluted hydrogel samples were obtained using a FEI Technai-12 transmission electron microscope at an accelerating voltage of 120 kV with a Gatan CCD camera. Micrographs were taken under dilute conditions to precisely measure the width of single fibrils within a dense network. All hydrogel samples were aged overnight at room temperature to ensure well-formed fibrillar morphologies. Sample preparation involved diluting incubated hydrogels at 1 wt % 20−30 times with deionized water, adding a 5 μL aliquot of the diluted gel on 400 mesh carbon-coated Cu grid, and blotting the excess by Whatman filter paper. Following this, 5 μL of 1 wt % uranyl acetate solution was then added onto the grid. Uranyl acetate serves as a negative stain for the hydrophilic self-assembled fibrils and leads to contrast enhancement. The grids were stained for 45 s−1 min before the excess stain was blotted. All grids were dried for a minimum of 1 h prior to imaging. Fibril width measurements were carried out using Image J,[74] an image analysis software from the National Institutes of Health (NIH).

Cryogenic Transmission Electron Microscopy (Cryo-TEM). A thin film (∼100 nm) of the preassembled hydrogel, incubated overnight, was transferred to a lacey carbon grid, blotted with filter paper, and plunged into liquid ethane. All samples were prepared using the environmentally controlled, automated Vitrobot from the FEI Company, Hillsboro, OR. In a typical sample preparation, the sample chamber was maintained at 25 °C and 40−50% relative humidity. Prior to plunging in liquid ethane, the sample was blotted with a filter paper 2−3 times for 1−2 s each. Following vitrification, the samples were transferred to a Gatan cryo-holder precooled to −175 °C before insertion into the electron microscope. Imaging was carried out in bright field mode at 120 kV in a Technai T12 electron microscope (FEI Co., Hillsboro, OR). During imaging, the temperature of the sample holder was maintained at −175 °C to inhibit sublimation of vitreous water.

Oscillatory Rheology. Rheological experiments were carried out on a TA Instruments AR 2000 controlled stress rheometer using parallel plate geometry and a 25 mm stainless steel tool. The rheometer was pre-equilibrated at 5 °C. Peptide and buffer solutions, also pre-equilibrated at 5 °C, were mixed in a 1:1 ratio,

and a 350 μL aliquot was quickly transferred to the rheometer plate. A gap of 500 μm was used for all measurements. S3 standard viscosity mineral oil (viscosity at 20 °C = 4.013 mPa·s) was placed around the sample to prevent water evaporation over time. In a typical experiment, the temperature was increased from 5 to 50 °C at a rate of 30 °C/min, causing the peptide solution to gel on the rheometer. The temperature was subsequently maintained at 50 °C for 1 h during a dynamic time sweep experiment performed at an angular frequency of 6 rad/s and a strain of 0.2%. Frequency sweeps from 0.1 to 100 rad/s and amplitude sweeps from 0.01 to 100% strain were subsequently performed to assess the frequency dependence and the linear viscoelastic region, respectively. All reported values of G' are a mean of three independent measurements on three distinct samples exhibiting a standard deviation of less than 10%. Error bars have not been shown since the rheometer measures moduli at different time points for each frequency sweep.

Acknowledgment. The identification of any commercial product or trade name does not imply endorsement or recommendation by the National Institute of Standards and Technology. This work was supported by NSF CHE0348323 (JPS-RPN), a Small Angle Neutron Scattering on Polymers and Complex Fluids Award (DJP-RAH, US Department of Commerce, # 70NANB7H6178), NIH 5RO1DEO16383, and the W. M. Keck Foundation for funding the College of Engineering Electron Microscopy Laboratory. This work utilized facilities supported in part by the National Science Foundation under Agreement No. DMR-0454672.

Supporting Information Available: Cryo-TEM image analysis and AFM data with image analysis. This material is available free of charge via the Internet at http://pubs.acs.org.

References and Notes

(1) Shibayama, M.; Tanaka, T.; Han, C. C. *J. Chem. Phys.* **1992**, *97*, 6829.
(2) Koizumi, S.; Annaka, M.; Borbely, S.; Schwahn, D. *Phys. B* (*Amsterdam, Neth.*) **2000**, *276*−*278*, 367.
(3) MacKintosh, F. C.; Kas, J.; Janmey, P. A. *Phys. Rev. Lett.* **1995**, *75*, 4425–4428.
(4) Karino, T.; Okumura, Y.; Zhao, C.; Kataoka, T.; Ito, K.; Shibayama, M. *Macromolecules* **2005**, *38*, 6161–6167.
(5) Farge, E.; Maggs, A. C. *Macromolecules* **1993**, *26*, 5041–5044.
(6) Morse, D. C. *Phys. Rev. E* **1998**, *58*, 1237–1240.
(7) Karim, A.; Douglas, J. F.; Horkay, F.; Fetters, L. J.; Satija, S. K. *Phys. B* (*Amsterdam, Neth.*) **1996**, *221*, 331–336.
(8) Caspi, A.; Elbaum, M.; Granek, R.; Lachish, A.; Zbaida, D. *Phys. Rev. Lett.* **1998**, *80*, 1106–1109.
(9) Kuznetsov, D. V.; Chen, Z. Y. *J. Chem. Phys.* **1998**, *109*, 7017.
(10) Fujita, H. *Polymer Solutions*; Elsevier Science: New York, 1990.
(11) Harnau, L.; Winkler, R. G.; Reineker, P. *J. Chem. Phys.* **1996**, *104*, 6355.
(12) Hammouda, B.; Worcester, D. *Biophys. J.* **2006**, *91*, 2237.
(13) Zhou, J.; Gregurick, S. K.; Krueger, S.; Schwarz, F. P. *Biophys. J.* **2006**, *90*, 544–551.
(14) Wang, L.; Bloomfield, V. A. *Macromolecules* **1991**, *24*, 5791–5795.
(15) Krueger, S.; Zaccai, G.; Wlodawer, A.; Langowski, J.; O'Dea, M.; Maxwell, A.; Gellert, M. *J. Mol. Biol.* **1990**, *211*, 211–20.
(16) Crichton, M.; Bhatia, S. *J. Appl. Crystallogr.* **2003**, *36*, 652–655.
(17) Korobko, A. V.; Jesse, W.; Lapp, A.; Egelhaaf, S. U.; van der Maarel, J. R. C. *J. Chem. Phys.* **2005**, 122.
(18) Borsali, R.; Nguyen, H.; Pecora, R. *Macromolecules* **1998**, *31*, 1548–1555.
(19) Won, Y. Y.; Davis, H. T.; Bates, F. S. *Science* **1999**, *283*, 960–963.
(20) Koehler, R. D.; Raghavan, S. R.; Kaler, E. W. *J. Phys. Chem. B* **2000**, *104*, 11035–11044.
(21) Pedersen, J. S.; Egelhaaf, S. U.; Schurtenberger, P. *J. Phys. Chem.* **1995**, *99*, 1299–1305.
(22) Engler, A. J.; Sen, S.; Sweeney, H. L.; Discher, D. E. *Cell* **2006**, *126*, 677.
(23) Pelham, R. J. Jr.; Wang, Y.-l. *Proc. Natl. Acad. Sci. U.S.A.* **1997**, *94*, 13661–13665.
(24) Stevens, M. M.; George, J. H. *Science* **2005**, *310*, 1135–1138.
(25) Nagarkar, R. P.; Hule, R. A.; Pochan, D. J.; Schneider, J. P. *J. Am. Chem. Soc.* **2008**, *130*, 4466–4474.
(26) Lee, K. Y.; Mooney, D. J. *Chem. Rev.* **2001**, *101*, 1869–1880.
(27) Peppas, N. A.; Huang, Y.; Torres-Lugo, M.; Ward, J. H.; Zhang, J. *Annu. Rev. Biomed. Eng.* **2000**, *2*, 9–29.
(28) Jia, X.; Kiick, K. L. *Macromol. Biosci.* **2009**, 9.
(29) Kirker, K. R.; Luo, Y.; Nielson, J. H.; Shelby, J.; Prestwich, G. D. *Biomaterials* **2002**, *23*, 3661–3671.
(30) Ishihara, M.; Nakanishi, K.; Ono, K.; Sato, M.; Kikuchi, M.; Saito, Y.; Yura, H.; Matsui, T.; Hattori, H.; Uenoyama, M. *Biomaterials* **2002**, *23*, 833–840.
(31) Song, J.; Malathong, V.; Bertozzi, C. R. *J. Am. Chem. Soc.* **2005**, *127*, 3366–3372.
(32) Song, J.; Saiz, E.; Bertozzi, C. R. *J. Am. Chem. Soc.* **2003**, *125*, 1236–1243.
(33) Freed, L. E.; et al. *J. Biomed. Mater. Res.* **1993**, *27*, 11−23.
(34) Bryant, S. J.; et al. *J. Biomed. Mater. Res., Part A* **2003**, *67A*, 1430−1436.
(35) Schmoekel, H. G.; et al. *Biotechnol. Bioeng.* **2005**, *89*, 253−262.
(36) Jeong, B.; Bae, Y. H.; Lee, D. S.; Kim, S. W. *Nature* **1997**, *388*, 860–861.
(37) Khattak, S. F.; Bhatia, S. R.; Roberts, S. C. *Tissue Eng.* **2005**, *11*, 974–983.
(38) Bryant, S. J.; Nuttelman, C. R.; Anseth, K. S. *J. Biomater. Sci., Polym. Ed.* **2000**, *11*, 439–457.
(39) Nguyen, K. T.; West, J. L. *Biomaterials* **2002**, *23*, 4307–4314.
(40) Pochan, D. J.; Schneider, J. P.; Kretsinger, J.; Ozbas, B.; Rajagopal, K.; Haines, L. *J. Am. Chem. Soc.* **2003**, *125*, 11802–11803.
(41) Schneider, J. P.; Pochan, D. J.; Ozbas, B.; Rajagopal, K.; Pakstis, L.; Kretsinger, J. *J. Am. Chem. Soc.* **2002**, *124*, 15030–15037.
(42) Ozbas, B.; Rajagopal, K.; Schneider, J. P.; Pochan, D. J. *Phys. Rev. Lett.* **2004**, *93*, 268106.
(43) Nair, C. M.; Vijayan, M.; Venkatachalapathi, Y. V.; Balaram, P. *J. Chem. Soc., Chem. Commun.* **1979**, *1979*, 1183–1184.
(44) Ozbas, B.; Kretsinger, J.; Rajagopal, K.; Schneider, J. P.; Pochan, D. J. *Macromolecules* **2004**, *37*, 7331–7337.
(45) Choo, D. W.; Schneider, J. P.; Graciani, N. R.; Kelly, J. W. *Macromolecules* **1996**, *29*, 355–366.
(46) Schaefer, D. W.; Zhao, J.; Brown, J. M.; Anderson, D. P.; Tomlin, D. W. *Chem. Phys. Lett.* **2003**, *375*, 369–375.
(47) Schaefer, D. W. *Science* **1989**, *243*, 1023–1027.
(48) Schmidt, G.; Nakatani, A. I.; Butler, P. D.; Han, C. C. *Macromolecules* **2002**, *35*, 4725–4732.
(49) Loizou, E.; Butler, P.; Porcar, L.; Kesselman, E.; Talmon, Y.; Dundigalla, A.; Schmidt, G. *Macromolecules* **2005**, *38*, 2047–2049.
(50) Krishnamoorti, R. *MRS Bull.* **2007**, *32*, 341–347.
(51) Picot, C. *Prog. Colloid Polym. Sci.* **1987**, *75*, 83–103.
(52) Kratz, K.; Hellweg, T.; Eimer, W. *Polymer* **2001**, *42*, 6631–6639.
(53) Beaucage, G. *J. Appl. Crystallogr.* **1995**, *28*, 717–728.
(54) Beaucage, G.; Schaefer, D. W. *J. Non-Cryst. Solids* **1994**, *172*, 797–805.
(55) Guinier, A.; Fournet, G. *Small Angle Scattering of X-rays*; Wiley-Interscience: New York, 1955.
(56) Hule, R. A.; Nagarkar, R. P.; Altunbas, A.; Ramay, H. R.; Branco, M. C.; Schneider, J. P.; Pochan, D. J. *Faraday Discuss.* **2008**, *139*, 251–264.
(57) Hammouda, B.; Ho, D. L.; Kline, S. *Macromolecules* **2004**, *37*, 6932–6937.
(58) Hammouda, B.; Horkay, F.; Becker, M. L. *Macromolecules* **2005**, *38*, 2019–2021.
(59) de Gennes, P. G. *Scaling Concepts in Polymer Physics*; Cornell University Press: Ithaca, NY, 1979.
(60) Ramachandran, S.; Trewhella, J.; Tseng, Y.; Yu, Y. B. *Chem. Mater.* **2006**, *18*, 6157–6162.
(61) Hjelm, R. P. *J. Appl. Crystallogr.* **1985**, *18*, 452–460.
(62) Burkoth, T. S.; Benzinger, T. L. S.; Urban, V.; Morgan, D. M.; Gregory, D. M.; Thiyagarajan, P.; Botto, R. E.; Meredith, S. C.; Lynn, D. G. *J. Am. Chem. Soc.* **2000**, *122*, 7883–7889.
(63) Jha, A. K.; Hule, R. A.; Jiao, T.; Teller, S. S.; Clifton, R. J.; Duncan, R. L.; Pochan, D. J.; Jia, X. *Macromolecules* **2009**, *42*, 537–546.
(64) Talmon, Y. *Colloids Surf.* **1986**, *19*, 237.
(65) Bellare, J. R.; Davis, H. T.; Scriven, L. E.; Talmon, Y. *J. Electron Microsc. Tech.* **1988**, *10*, 87–111.

(66) Cui, H.; Hodgdon, T. K.; Kaler, E. W.; Abezgauz, L.; Danino, D.; Lubovsky, M.; Talmon, Y.; Pochan, D. J. *Soft Matter* **2007**, *3*, 945–955.
(67) Yucel, T.; Micklitsch, C. M.; Schneider, J. P.; Pochan, D. J. *Macromolecules* **2008**, *41*, 5763–5772.
(68) Haines-Butterick, L.; Rajagopal, K.; Branco, M.; Salick, D.; Rughani, R.; Pilarz, M.; Lamm, M. S.; Pochan, D. J.; Schneider, J. P. *Proc. Natl. Acad. Sci. U.S.A.* **2007**, *104*, 7791–7796.
(69) Appell, J.; Porte, G.; Khatory, A.; Kern, F.; Candau, S. J. *J. Phys. II* **1992**, *2*, 1045–1052.
(70) Porte, G.; Gomati, R.; El Haitamy, O.; Appell, J.; Marignan, J. *J. Phys. Chem.* **1986**, *90*, 5746–5751.
(71) Khatory, A.; Kern, F.; Lequeux, F.; Appell, J.; Porte, G.; Morie, N.; Ott, A.; Urbach, W. *Langmuir* **1993**, *9*, 933–939.
(72) Glinka, C. J.; Barker, J. G.; Hammouda, B.; Krueger, S.; Moyer, J. J.; Orts, W. J. *J. Appl. Crystallogr.* **1998**, *31*, 430–445.
(73) Kline, S. R. *J. Appl. Crystallogr.* **2006**, *39*, 895–900.
(74) Rasband, W. S. *ImageJ*; U.S. National Institutes of Health: Bethesda, MD, 1997−2006; http://rsb.info.nih.gov/ij/.